

Research Article

Attenuation Law of Stress Waves in Cracked Rock Mass under Different Confining Pressures

Xiaoming Lou ^{1,2}, Rui Luo,^{1,2} and Jin Yu³

¹College of Zijin Mining, Fuzhou University, Fuzhou, Fujian 350108, China

²Institute of Blasting Technology, Fuzhou University, Fuzhou 350116, China

³Institute of Geotechnical Engineering, Huaqiao University, Xiamen 361021, China

Correspondence should be addressed to Xiaoming Lou; 331261323@qq.com

Received 25 March 2019; Accepted 13 June 2019; Published 1 July 2019

Academic Editor: Rafael J. Bergillos

Copyright © 2019 Xiaoming Lou et al. This is an open access article distributed under the Creative Commons Attribution License, which permits unrestricted use, distribution, and reproduction in any medium, provided the original work is properly cited.

Through theoretical analysis and indoor model tests, this paper explores the attenuation law of stress waves in the intact confined rock mass and cracked rock mass under different confining pressures, especially the relationship between the stress attenuation coefficient, crack width, and crack angle, respectively. The tests were carried out on a triaxial test system for deep rock mass, which supports both static and dynamic loading. The research results show that the physical attenuation of the stress wave in the intact rock mass first decreases and then increases with the increase of the confining pressure and decreases with the increase of crack width. The attenuation coefficient of stress waves in the cracked rock mass depends on the crack angle and crack width. Specifically, the coefficient is negatively correlated with crack width; under no confining pressure, the coefficient decreases with the increase of the crack angle; when the confining pressure is on a moderate level, the coefficient increases with the crack angle; when the confining pressure exceeds the uniaxial intensity by 34%, the coefficient decreases again with the increase of the crack angle. The theoretical propagation equation of stress waves at the crack, which was derived from the propagation attenuation mechanism of stress waves in the cracked rock mass, was proved feasible through the comparison against the experimental results.

1. Introduction

The propagation of stress waves will weaken the physical-mechanical strength and stability of the rock mass. The stress wave obeys different attenuation laws in shallow and deep rock masses. The deep rock mass suffers higher ground stress than the shallow one, creating a broader range of cracks. The difference affects the reliable calculation of the surrounding rock stability. Therefore, it is very meaningful to explore the propagation of stress waves in the cracked rock mass under confining pressure.

The earliest theory on the stress wave propagation in the cracked rock mass is the discontinuous deformation analysis (DDA) [1], which focuses on the stress wave passing through discontinuities in cracked rock masses. Many other theories have been extended from the DDA, including the method of characteristics (MC) [2], the scattering matrix method (SMM) [3], and the virtual wave source (VWS) method [4].

In addition, Bandis et al. [5] proposed a hyperbolic Barton–Bandis model to describe the nonlinear deformation features of penetration cracks caused by the stress wave.

Many experiments have been performed on the stress wave propagation in the cracked rock mass. For instance, Li and Ma [6] carried out a split-Hopkinson pressure bar (SHPB) test, revealing that the stress wave propagation is affected by the presence of closed cracks, and the stress attenuation coefficient is closely related to the crack width. Reza et al. [7] examined the effects of distance and crack angle on the propagation of cylindrical SH waves. Based on the linear elastic model of discontinuous displacement, Pyrak-Nolte [8] derived the attenuation coefficient of the stress wave at the crack. Jin et al. [9] studied the propagation law of stress waves vertically incident on the cracked rock mass. Tingting et al. [10] numerically analyzed the attenuation law of stress waves through parallel cracks and obtained the relationship between the attenuation coefficient

and the number of cracks. Yuan et al. [11] obtained the method which changes the mineral's permeability via stress waves.

The confining pressure directly bears on the mechanical properties of the surrounding rock. Many have simulated the mechanical properties of the rock mass under dynamic and static loads. For example, Fan and Sun [12] studied the attenuation law of the stress wave passing through a single crack under the initial ground stress, using the displacement discontinuity method (DDM). Through an SHPB test, Li [13] found that the strength features of the rock mass are significantly different under different dynamic and static loads.

To sum up, the existing studies mainly concentrate on the effects of confining pressure on the mechanical properties of the rock mass. There are only a few reports on the propagation law of stress waves in the cracked rock mass under confining pressure. To make up for this gap, this paper probes into the effects of crack angle and crack width on stress wave propagation in rock masses under different confining pressures, through both theoretical analysis and indoor model tests. The results calculated from the attenuation equation were compared with the experimental results. The research findings shed new light on the propagation and attenuation of stress waves in cracked rock masses.

2. Theoretical Analysis

2.1. Attenuation of Stress Waves in Intact Rock Mass. The stress wave attenuates both geometrically and physically as it propagates through the rock mass [14]. The geometric attenuation is resulted from the spatial distribution of the stress wave energy, and the physical attenuation is caused by the friction on the internal crack surface of the propagation medium. The attenuation equation of the stress wave in the rock mass can be established by combining the two types of attenuations:

$$v_r = v_0 \left(\frac{r_0}{r} \right)^{1/2} e^{-\eta r}. \quad (1)$$

2.2. Stress Wave Attenuation Equation. Under the joint effects of stress waves and confining pressure, the stress conditions of cracks were derived through the 2D implication of the interaction between the stress wave and the cracks (Figure 1).

According to the equilibrium condition of the fracture force, the static normal stress and the tangential stress on the crack surface under the confining pressure can be, respectively, expressed as

$$\begin{aligned} \sigma_\theta &= \lambda \sigma_1 \sin^2 \theta + \sigma_1 \cos^2 \theta, \\ \tau_\theta &= 0.5 \sigma_1 \cdot (1 - \lambda) \sin 2\theta. \end{aligned} \quad (2)$$

Considering the dynamic relationship between the stress wave and the crack, it is assumed that the stress wave generated by source O of gap S, i.e., the incident wave, is perpendicular to the horizontal ground stress (Figure 2).

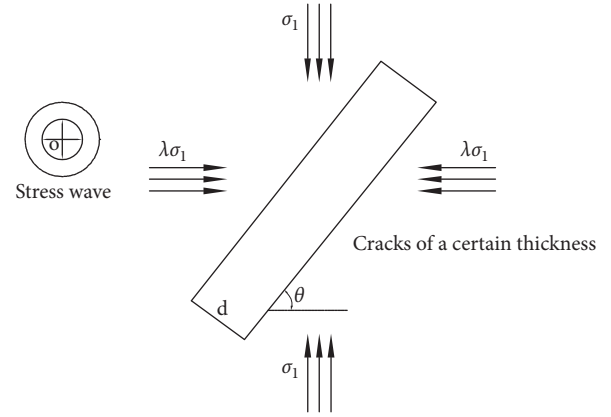


FIGURE 1: Stress conditions of cracks under stress waves and confining pressure.

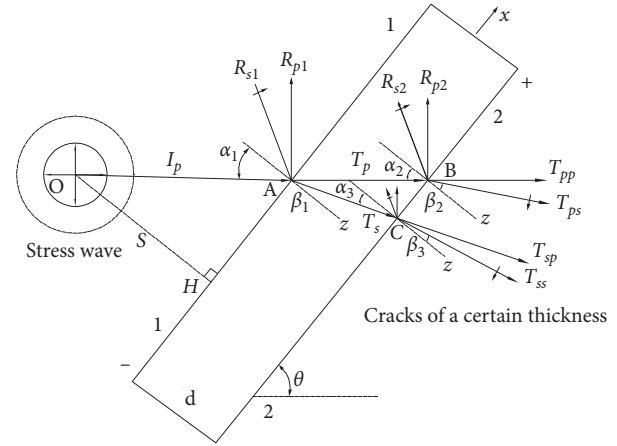


FIGURE 2: Interaction between the stress wave and the cracks.

In Figure 2, the stress wave is translected when it passes through a crack of a certain width. In light of the stress equilibrium condition, wave front momentum conservation, and interaction between the stress wave and the cracks, the stress and particle vibration velocity on the two sides of the 1-1 crack surface can be expressed as [15]

$$\sigma_1^- = z_p v_{I_p} \cos(2\beta_1) + z_p v_{R_p} \cos(2\beta_1) - z_s v_{R_s} \sin(2\beta_1), \quad (3)$$

$$\tau_1^- = \left(z_p v_{I_p} - z_p v_{R_p} \right) \left(\frac{\sin(2\beta_1) \tan \beta_1}{\tan \alpha_1} \right) - z_s v_{R_s} \cos(2\beta_1), \quad (4)$$

$$\sigma_1^+ = z_p v_{T_p} \cos(2\beta_1) + z_s v_{T_s} \sin(2\beta_1), \quad (5)$$

$$\tau_1^+ = z_p v_{T_p} \left(\frac{\sin(2\beta_1) \tan \beta_1}{\tan \alpha_1} \right) - z_s v_{T_s} \cos(2\beta_1), \quad (6)$$

$$v_n^- = v_{I_p} \cos \alpha_1 - v_{R_p} \cos \alpha_1 + v_{R_s} \sin \beta_1, \quad (7)$$

$$v_i^- = v_{I_p} \sin \alpha_1 - v_{R_p} \sin \alpha_1 + v_{R_s} \cos \beta_1, \quad (8)$$

$$v_n^+ = v_{T_p} \cos \alpha_1 + v_{T_s} \sin \beta_1, \quad (9)$$

$$v_i^+ = v_{T_p} \sin \alpha_1 - v_{T_s} \cos \beta_1, \quad (10)$$

where σ^- and σ^+ are the normal stresses on the two sides of the 1-1 crack surface, respectively; τ^- and τ^+ are the tangential stresses on the two sides of the 1-1 crack surface, respectively; v_{I_p} is the vibration velocity of the particle under the incident wave; v_{T_p} and v_{T_s} are the vibration velocities of the particle under the transmitted P and S waves, respectively; v_{R_p} and v_{R_s} are the particle vibration velocities of the reflected P and S waves, respectively; and z_p and z_s are the P and S wave impedances of the rock mass, respectively. Here, $z_p = \rho c_p$ and $z_s = \rho c_s$, with ρ being the rock density, c_p being the propagation velocity of P waves in the rock mass, and c_s being the propagation velocity of S waves in the rock mass.

According to the DDA [1], the stress is continuous on both sides of the 1-1 crack surface, but the deformation is not continuous. The normal deformation and tangential deformation on the 1-1 crack surface can be, respectively, expressed as

$$u_n^- - u_n^+ = \frac{\sigma_\theta + \sigma_1^+}{k_{ni} + \langle (\sigma_\theta + \sigma_1^+) / d_{ma} \rangle}, \quad (11)$$

$$u_\tau^- - u_\tau^+ = \frac{\tau_\theta + \tau_1^+}{k_s}, \quad (12)$$

where u_n^- and u_n^+ are the normal displacements on the two sides of the 1-1 crack surface, respectively; u_τ^- and u_τ^+ are the tangential displacements on the two sides of the 1-1 crack surface, respectively; k_{ni} is the initial normal stiffness of the crack; and d_{ma} is the crack with the maximum allowable closing amount. Both k_{ni} and d_{ma} satisfy the BB model [5].

The generalized normal stiffness k_g of the crack under confining pressure can be calculated as [16]

$$k_g = \frac{\langle k_{ni} + ((\sigma_\theta + \sigma_1^+) / d_{ma}) \rangle^2}{k_{ni}}. \quad (13)$$

Considering the geometric attenuation and physical attenuation of the stress wave, the following can be derived from equations (1) and (3)~(13):

$$\begin{bmatrix} v_{R_{p1}}(i) \\ v_{R_{s1}}(i) \end{bmatrix} = Av_{I_p}(i) \left(\frac{r_0}{r} \right)^{1/2} e^{-\eta r} + CB^{-1} \begin{bmatrix} v_{T_{p1}}(i) \\ v_{T_{s1}}(i) \end{bmatrix}, \quad (14)$$

$$\begin{bmatrix} v_{T_{p1}}(i+1) \\ v_{T_{s1}}(i+1) \end{bmatrix} = DG^{-1}v_{I_p}(i) \left(\frac{r_0}{r} \right)^{1/2} e^{-\eta r} + EG^{-1} \begin{bmatrix} v_{R_{p1}}(i) \\ v_{R_{s1}}(i) \end{bmatrix} + FG^{-1} \begin{bmatrix} v_{T_{p1}}(i) \\ v_{T_{s1}}(i) \end{bmatrix}, \quad (15)$$

where

$$\begin{aligned} A &= \frac{1}{z_p z_s \langle \cos^2(2\beta_1) - \sin^2(2\beta_1) \tan \beta_1 \cot \alpha_1 \rangle} \begin{bmatrix} z_p z_s \langle \sin^2(2\beta_1) \tan \beta_1 \cot \alpha_1 - \cos^2(2\beta_1) \rangle \\ 2z_p^2 \sin(2\beta_1) \cos(2\beta_1) \tan \beta_1 \cot \alpha_1 \end{bmatrix}, \\ B &= \begin{bmatrix} z_p \cos(2\beta_1) & -z_s \sin(2\beta_1) \\ -z_p \sin(2\beta_1) \tan \beta_1 \cot \alpha_1 & -z_s \cos(2\beta_1) \end{bmatrix}, \\ C &= \begin{bmatrix} z_p \cos(2\beta_1) & z_s \sin(2\beta_1) \\ z_p \sin(2\beta_1) \tan \beta_1 \cot \alpha_1 & -z_s \cos(2\beta_1) \end{bmatrix}, \\ D &= \begin{bmatrix} k_g \Delta t \cos \alpha_1 \\ k_s \Delta t \sin \alpha_1 \end{bmatrix}, \\ E &= \begin{bmatrix} -k_g \Delta t \cos \alpha_1 & k_g \Delta t \sin \beta_1 \\ k_s \Delta t \sin \alpha_1 & k_s \Delta t \cos \beta_1 \end{bmatrix}, \\ F &= \begin{bmatrix} -k_g \Delta t \cos \alpha_1 + z_p \cos(2\beta_1) & -k_g \Delta t \sin \beta_1 + z_s \sin(2\beta_1) \\ -k_s \Delta t \sin \alpha_1 + z_p \sin(2\beta_1) \tan \beta_1 \cot \alpha_1 & k_s \Delta t \cos \beta_1 - z_s \cos(2\beta_1) \end{bmatrix}, \\ G &= \begin{bmatrix} z_p \cos(2\beta_1) & z_s \sin(2\beta_1) \\ z_p \sin(2\beta_1) \tan \beta_1 \cot \alpha_1 & -z_s \cos(2\beta_1) \end{bmatrix}. \end{aligned} \quad (16)$$

Equations (14) and (15) can be solved by Python programming, yielding the particle vibration velocity v_{T_p} of the transmitted wave. The P wave is the main cause of rock cracking. The attenuation coefficient C_{p1} of the stress wave on the 1-1 crack surface can be calculated as

$$C_{p1} = \frac{\max|v_{T_p}(i)|}{\max|v_{I_p}(i)|}. \quad (17)$$

The P wave attenuates as it propagates through the crack:

$$v_B = v_A \left(\frac{1}{d/\cos \alpha_2} \right)^{1/2} e^{-\eta r}. \quad (18)$$

The attenuation coefficient C_{p2} of the stress wave on the 2-2 crack surface can be obtained similarly as

$$C_{p2} = \frac{\max|v_{T_{pp}}(i)|}{\max|v_{T_B}(i)|} = \frac{\max|v_{T_{pp}}(i)|}{\max|v_A((1/(d/\cos \alpha_2)))^{1/2} e^{-\eta r}|}. \quad (19)$$

Thus, the total attenuation coefficient of the stress wave passing through different crack widths and angles under different confining pressure conditions can be defined as

$$T = C_{p1} \cdot C_{p2}. \quad (20)$$

3. Model Test

3.1. Principle and Test System. With the advantages of repeatable monitoring, low cost, and high precision, the strain gauge is an important tool to measure stress [17, 18]. During the measurement, the strain gauge at each measuring point is deformed when the specimen is under dynamic stress, causing a change in resistance. The resistance signal is converted into a voltage signal, the voltage variation pattern is displayed, and finally, the stress of the specimen is obtained by inverse calculation:

$$P = \frac{4UE \times 10^6}{kU_0 nG}, \quad (21)$$

where P is the specimen stress (MPa), U is the output voltage (V), k is the sensitivity coefficient of the instrument, U_0 is the bridge box pressure, E is the elastic modulus of the specimen, n is the number of strain gauges, and G is the instrument gain.

Our model test uses a 120~50AA concrete strain gauge, a 120 Ω resistance, a grid size of 50.0 mm \times 4.0 mm, and a sensitivity coefficient of $2.08 \pm 1\%$. The 50 mm \times 50 mm \times 5 mm strain brick was prepared by the following steps: First, the brick was polished with sandpaper at the angle of 45°, ensuring that the brick surface is smooth, without any inlaid gravel. Then, the strain gauge was pasted quickly to the correct position with 502 glue. The excess glue was squeezed out to achieve good contact between the gauge and the brick.

To prevent signal interference, the circuits were connected via shielded cables. The KD6009A strain amplifier and KD7901 bridge box were selected to process the

measured signals. The strain brick was preburied in the concrete model to collect dynamic stress signals and treated with moisture to avoid corrosion. The test system is illustrated in Figure 3.

3.2. Loading Equipment and Similar Material. Our indoor model test examined the propagation and attenuation of stress waves in the intact rock mass and the rock mass cracked under high confining stress. The test was performed on the triaxial test system for deep rock mass, which supports both static and dynamic loading. As shown in Figure 4, the 200 mm \times 200 mm \times 200 mm specimen was mold-casted and coated with Vaseline to eliminate the end effect. The test system can implement three-way uniform loading on the specimen and apply a dynamic load in the z -axis direction. The static load peaks at 60 MPa. The test equipment has a gravity compensation design, and the weight of the specimen is negligible.

The model test targets a rock cracked under high confining stress. A total of five typical deep mining areas were selected, and the mechanical parameters of the surrounding rock in these areas were subjected to comprehensive analysis. Inspired by the Froude similarity theory, the test stress ratio was set to 10. The physical-mechanical parameters of the original rock and the similar material are listed in Table 1. As shown in the table, the mix ratio of the similar material is as follows: cement : sand : water : cement molding agent = 2 : 4.7 : 1 : 0.027. Thus, the similar material is dominantly cement mortar, with a few additive materials. Note that the sand was screened by a 24-mesh sieve.

In addition, the cracks were simulated as mica flakes. The normal initial stiffness k_{ni} of the cracks was obtained through normal loading tests, and the shear stiffness of the cracks was derived from the normal stiffness by $k_s = k_{ni}/2(1 - \mu)$ [19], where μ is Poisson's ratio. The confining pressures of the intact rock mass were simulated at 0 MPa, 2 MPa, 4 MPa, 6 MPa, 8 MPa, and 10 MPa, respectively, and those of the deep rock masses at 0 MPa, 20 MPa, 40 MPa, 60 MPa, 80 MPa, and 100 MPa, respectively.

3.3. Experimental Protocol and Validation. The stress wave was generated by the dynamic stress axis of the test system according to the Jones–Wilkens–Lee (JWL) equation of state. The stress was simulated with a peak value of 450 kN at the bottom. The static load was applied around the model to simulate the underground confining pressure. Meanwhile, the dynamic load was imposed by the dynamic stress axis, which also collected the strain of each measuring point in the specimen.

The change of the stress wave after passing through the crack was quantified by stress and strain. Due to the damping effect of the crack, the peaks of stress and strain mostly appeared in the first wave of the time-history curve. Hence, the peak ratio between the precrack stress and the postcrack stress can be defined as the attenuation factor. Since the stress wave reflected at the crack boundary may interfere in the collected data, the distance between the measuring point and the crack was reasonably selected, to

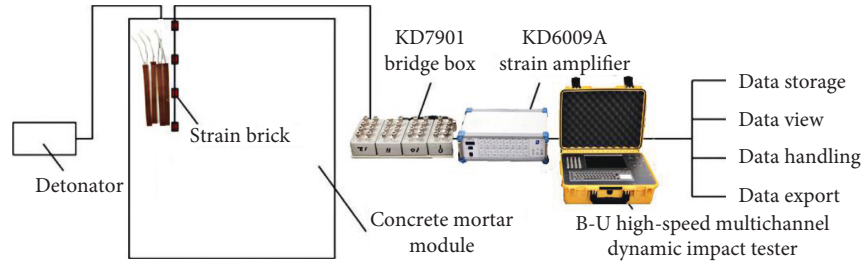


FIGURE 3: Stress-monitoring test system.

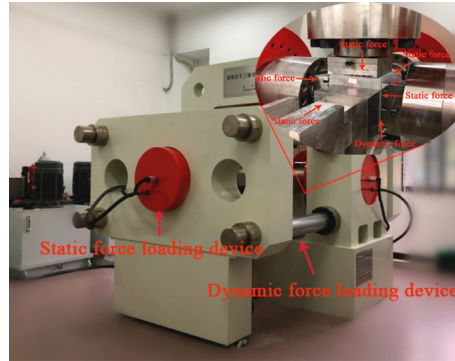


FIGURE 4: Triaxial test system.

TABLE 1: Physical-mechanical parameters of the original rock and the similar material.

Category	Compressive strength (MPa)	Tensile strength (MPa)	Elastic modulus (GPa)	Internal friction angle (°)	Cohesion (MPa)	Poisson's ratio	Density (kg·m ⁻³)
Original rock	170.00	16.00	40.000	35.0	40.00	0.346	2.800
Model	17.53	1.71	1.099	30.3	2.12	0.301	2.235

eliminate the effect of the reflected wave on the peak of the first wave. The wave propagation was not affected by surface delamination because the vibrating rods were used to ensure the uniform density of the specimen. The relative positions of the measuring points and the cracks are displayed in Figure 5.

Measuring points 1~3 were selected to verify the uniformity of the specimens. The time-history curves of the strain of these points without confining pressure are shown in Figure 6.

As shown in Figure 6, the peak strains of points 1, 2, and 3 were -364.75×10^{-6} , -327.26×10^{-6} , and -290.48×10^{-6} , respectively, and the three points shared the same decreasing trend with the increase of the distance. This means the stress wave propagated evenly in the specimen, and the model could apply to the simulation of the deep rock mass.

4. Analysis on Intact Rock Mass

In the model test, the strain-measuring points were arranged at an equal interval of 33 mm along the propagation direction of the stress wave. As shown in Figure 7, the dynamic

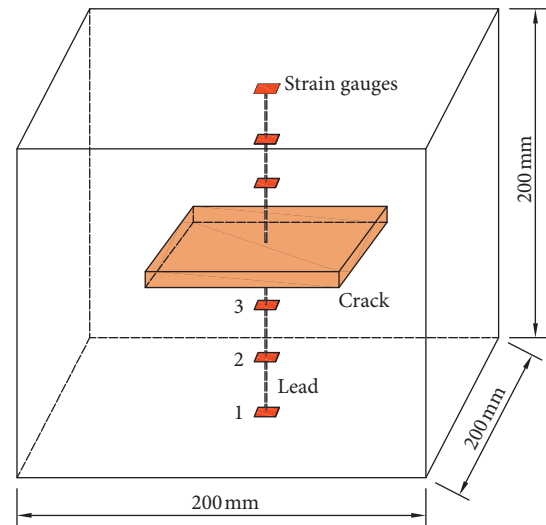


FIGURE 5: Relative positions of measuring points and cracks.

stress was loaded from the bottom, and a 50 kN preload was applied on the top. The model was applied with a confining pressure of 2 MPa.

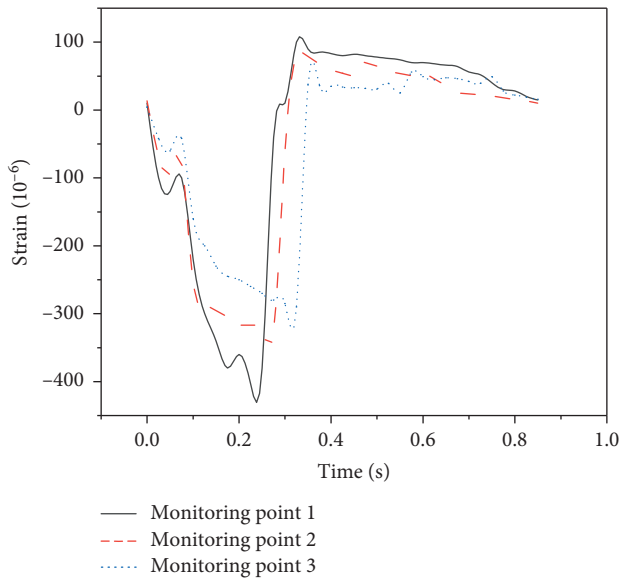


FIGURE 6: Time-history curves of the strain without confining pressure.

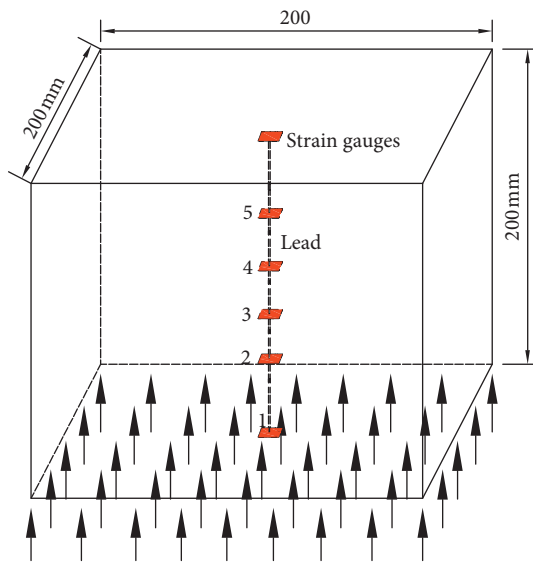


FIGURE 7: Sketch map of stress wave propagation in the intact rock mass.

The time history of strain was recorded during the loading of each measuring point. For simplicity, the absolute value of the peak strain was selected for further analysis. The measured peak stresses of the six measuring points were recorded.

As mentioned above, the stress wave attenuated both geometrically and physically. The geometric attenuation depends on the wave front diffusion and has nothing to do with the propagation medium or boundary conditions [20]. Since no attenuation existed at 0 mm, the data at this measuring point were excluded from the analysis. After removing the geometric attenuation of 40~200 mm, the physical attenuation of the stress wave through the intact rock

mass was obtained at different confining pressures (Figure 8).

Taking the waveform measured at point 2 as the incident wave and the waveform at point 6 as the projected wave, the attenuation coefficient of the stress wave in the intact rock mass was defined as the peak strain ratio between the projected wave and the incident wave. As the confining pressure increased from 0 to 10 MPa, the attenuation coefficient of the stress wave propagating from point 2 to point 6 changed gradually from 0.433, 0.395, 0.309, 0.357, 0.395, to 0.416. The relationship between the attenuation coefficient and the confining pressure is recorded in Figure 9.

Based on the data in Figure 9, the relationship between the physical attenuation coefficient of the stress wave A and the confining pressure B can be determined through regression analysis:

$$\eta = 0.435 + 0.003\sigma - 0.02\sigma^2 + 0.005\sigma^3. \quad (22)$$

The analysis results demonstrate the correlation between the physical attenuation of the stress wave in intact rock and the confining pressure. With the increase of the confining pressure, the physical attenuation coefficient of the stress wave decreased first and then increased. This trend is attributable to the presence of microcracks in the intact specimen. Upon the arrival of the stress wave, the microcrack slipped and closed when the confining pressure was no greater than 4 MPa. The stress wave was partially converted into heat energy, leading to a decrease of the stress peak. The physical attenuation coefficient decreased with the number of small, open cracks. When the confining pressure increased from 4 MPa to 10 MPa (i.e., 23% to 57% of the uniaxial compressive strength of the material), new cracks appeared with the expansion of the closed crack inside the material, causing sliding under the stress wave; this phenomenon is verified in the previous research [21]. Then, the physical stress attenuation coefficient increased with the number of small, open cracks. This phenomenon agrees with the previous research too [22].

5. Analysis on Cracked Rock Mass

5.1. Effects of Crack Width on Stress Propagation. In the model test, the effect of crack width on the stress wave propagation was simulated at different crack widths, namely, 5 mm, 10 mm, 20 mm, 30 mm, and 40 mm (Figure 10).

Without changing other parameters, the initial cracking stiffness was set to 14.1 GPa/m, 14.8 GPa/m, 15.3 GPa/m, 15.9 GPa/m, and 16.4 GPa/m, respectively, and the maximum allowable closing amount to 1.5 mm, 2 mm, 4 mm, 7 mm, and 9 mm, respectively. The dynamic load was applied from the bottom and the static load around the specimen to simulate different confining pressures. Here, the attenuation coefficient is defined as the specific gravity ratio between the postcrack peak stress and the precrack peak stress. The variations of the attenuation coefficient with crack widths and confining pressures are shown in Figures 11 and 12, respectively.

It can be seen from Figure 11 that as the thickness increases, the attenuation coefficient of the stress wave shows a

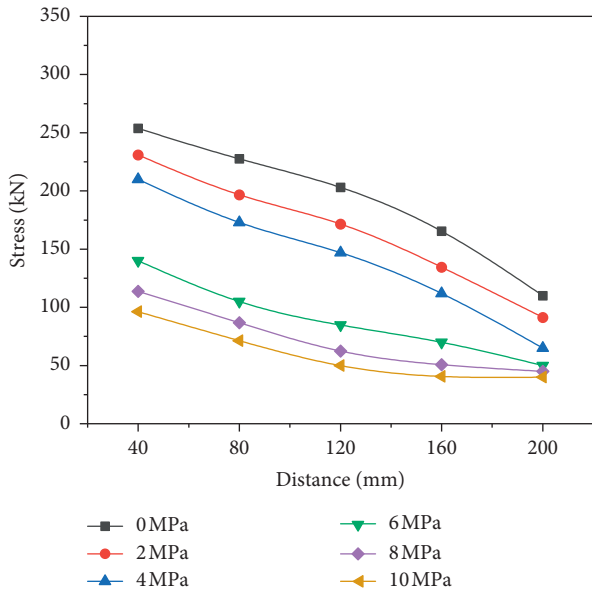


FIGURE 8: Physical attenuation law of stress waves in intact rock under different confining pressures.

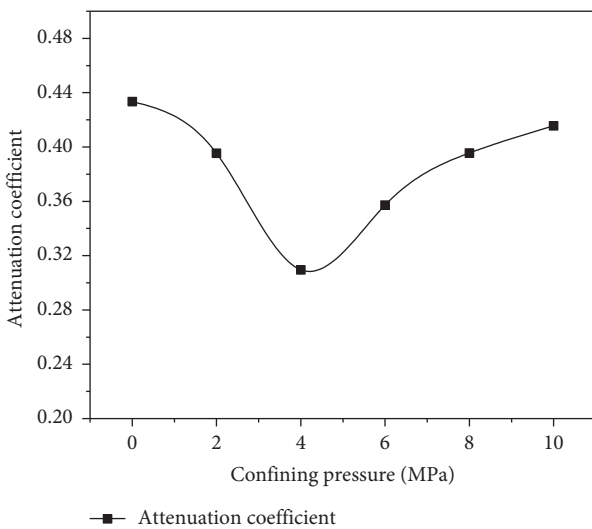


FIGURE 9: Variation law of the physical attenuation coefficient under different confining pressures.

decreasing trend. This is because the increase of the crack width leads to the decrease of the strength of the rock mass, and the cracking effect of the crack on the stress wave is enhanced, which accelerates the attenuation of the stress wave. As the crack width increases, the stress is blocked into energy form at the crack, and the attenuation coefficient of the stress wave at the crack decreases with the increase of the crack width. It can be seen from Figure 12 that the attenuation law of the stress at the crack increases first and then increases with the increase of the confining pressure. When the confining pressure is less than 4 MPa, the microcrack in the rock mass increases with the confining pressure. Being compacted consumes a lot of energy, resulting in reduced stress. When the confining pressure is greater than 4 MPa, as

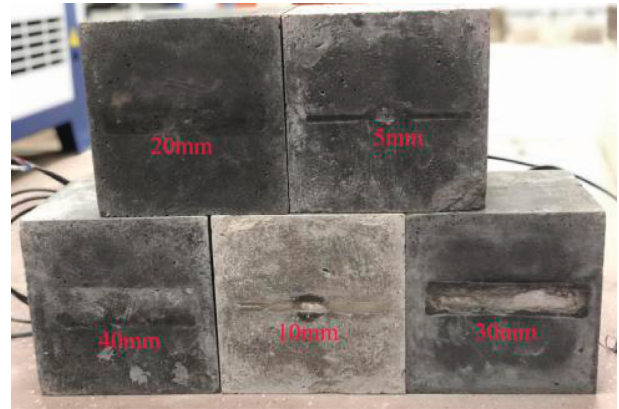


FIGURE 10: Different thickness models.

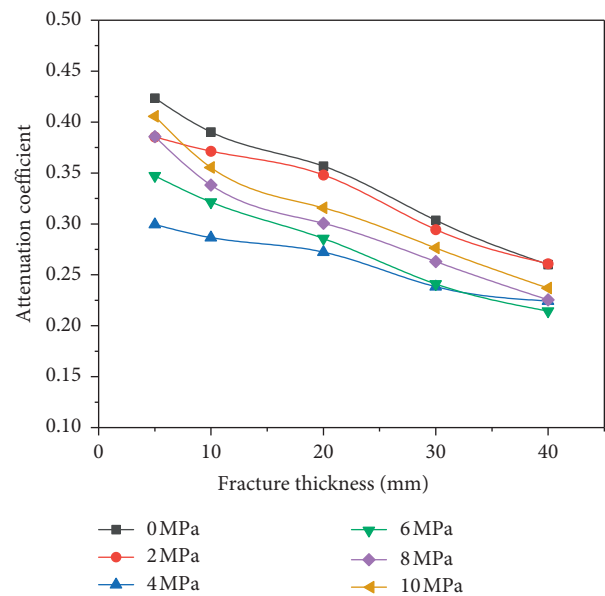


FIGURE 11: Variation of the attenuation coefficient with crack widths.

the confining pressure increases, the barrier effect on the stress wave is reduced after the fracture is compacted, and the stress wave attenuation coefficient increases.

5.2. Effects of Crack Angle on Stress Propagation. The projection coefficient of the stress wave was defined as the ratio of precrack peak pressure and postcrack peak pressure. Here, the pressures are measured at different crack angles (i.e., 15°, 30°, 45°, 60°, 75°, and 90°) and the same crack width (5 mm) (Figure 13).

Under the confining pressures of 2 MPa, 4 MPa, 6 MPa, 8 MPa, and 10 MPa and the bottom stress of 450 kN, the data of each measuring point were collected for further analysis (Figures 14 and 15).

As shown in Figures 14 and 15, when the confining pressure was 0 MPa, the stress wave attenuation coefficient decreased with the increase of the crack angle. When the confining pressure increased from 0 to 4 MPa, the stress

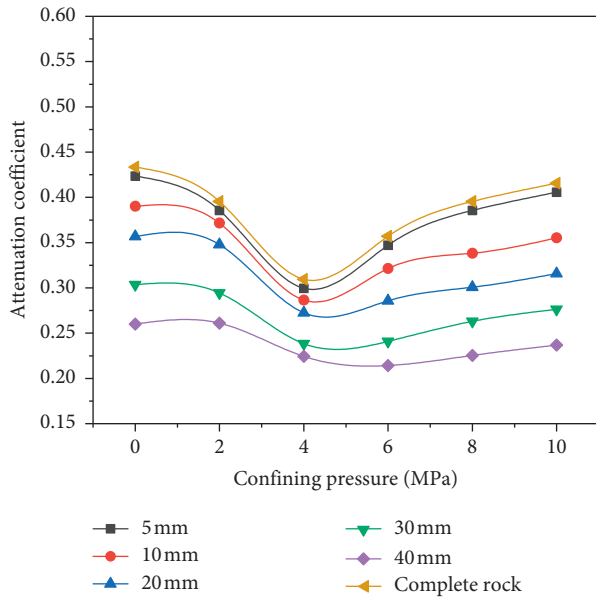


FIGURE 12: Variation of the attenuation coefficient with confining pressures.

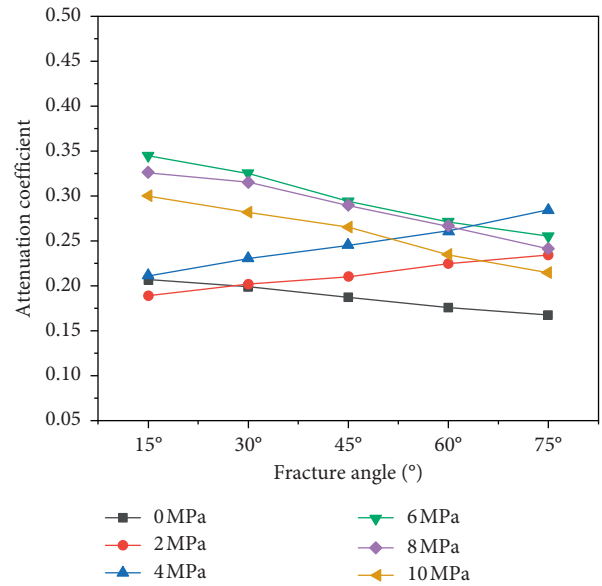


FIGURE 14: Variation of the stress attenuation coefficient with crack angles.



FIGURE 13: Multiangle test model.

wave attenuation coefficient increased with the crack angle. When the confining pressure exceeded 6 MPa, or 34% of the uniaxial compressive strength of the specimen, the stress wave attenuation coefficient decreased with the increase of the crack angle.

The reason for the above phenomenon is that when the confining pressure increased from 0 to 4 MPa, the stiffness of the crack increased, which dampened the barrier effect of the crack on the stress, stimulating a growth in stress attenuation coefficient. When the confining pressure increased from 6 MPa to 10 MPa, numerous microcracks were generated inside the rock mass, and the stress wave was converted into energy, leading to a decline in the stress attenuation coefficient.

5.3. Comparison between Theoretical and Experimental Results. The model test values were contrasted with the theoretical results at the crack width of 5 mm, the crack

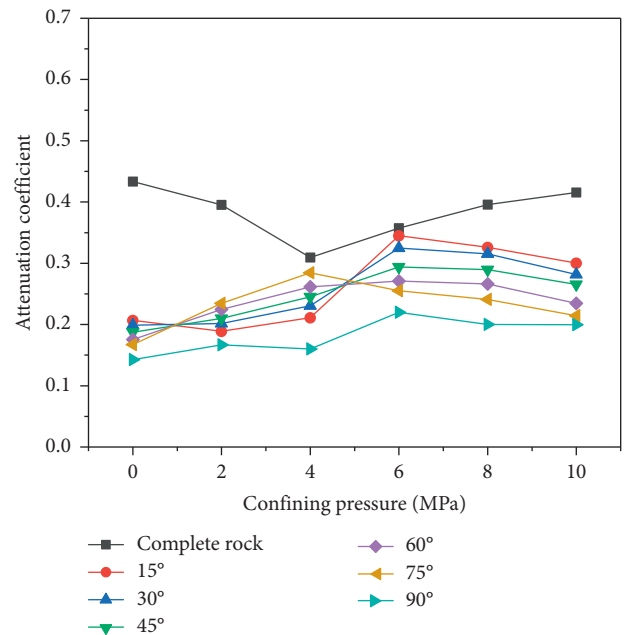


FIGURE 15: Variation of the stress attenuation coefficient with confining pressures.

angles of 30° and 75°, and the peak loading stress of 450 kN. The comparison results are shown in Figure 16.

Figure 16 manifests that the attenuation coefficient of the stress wave in the cracked rock mass under different confining pressures agrees well with the measured values, which confirms the feasibility of the theoretical calculation. The theoretical value was slightly larger than the measured value, for the theoretical analysis only considering the radial stress rather than the tangential stress. Besides, the theoretical calculation ignored the stress wave energy consumed by the

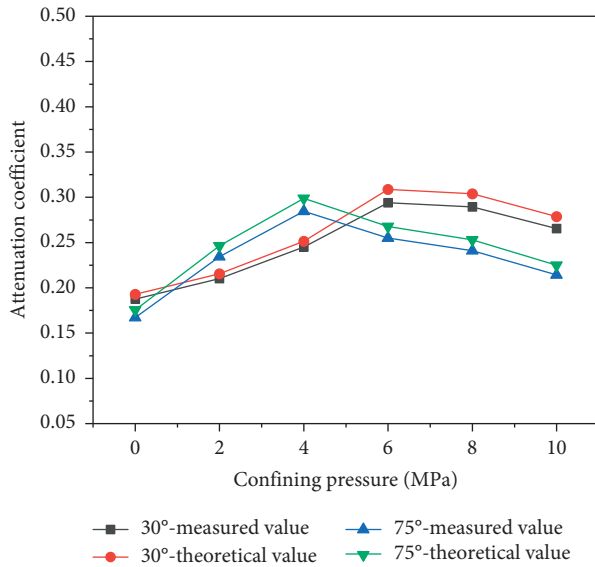


FIGURE 16: Comparison between theoretical and experimental stress attenuation coefficients.

crack expansion. As a result, when the confining pressure exceeded 6 MPa, many microcracks appeared in the model, which amplified the deviation between the theoretical and measured values. The maximum error is 4.7% less than 5%, so the overall error is within the allowable error range.

6. Conclusions

Through theoretical analysis and model tests, this paper discloses the relationship between stress wave propagation attenuation, crack width, and crack angle under different confining pressures. The main conclusions are put forward as follows:

- (1) The theoretical propagation equation of the stress wave at the crack, which was derived from the propagation attenuation mechanism of the stress wave in the cracked rock mass, was proved feasible through the comparison against the experimental results.
- (2) The relationship between confining pressure and physical attenuation in the rock mass can be described by a polynomial function: with the increase of the confining pressure, the physical attenuation of the stress wave first decreases and then increases.
- (3) The attenuation coefficient of the stress wave in the cracked rock mass depends on the crack angle and crack width. Specifically, the coefficient is negatively correlated with crack width; under no confining pressure, the coefficient decreases with the increase of the crack angle; when the confining pressure is on a moderate level, the coefficient increases with the crack angle; when the confining pressure exceeds the uniaxial intensity by 34%, the coefficient decreases again with the increase of the crack angle.

Data Availability

The datasets used or analyzed during the current study are available from the corresponding author on reasonable request.

Conflicts of Interest

The authors declare that there are no conflicts of interest regarding the publication of this paper.

Acknowledgments

This research work was supported by the National Natural Science Foundation of China under Grant nos. 51679093 and 51374112.

References

- [1] M. Schoenberg, "Elastic wave behavior across linear slip interfaces," *Journal of the Acoustical Society of America*, vol. 68, no. 5, pp. 1516–1521, 1980.
- [2] J. G. Caj and J. Zhao, "Effects of multiple parallel fractures on apparent attenuation of stress waves in rock masses," *International Journal of Rock Mechanics and Mining Sciences*, vol. 37, no. 4, pp. 661–682, 2000.
- [3] K. Aki and P. G. Richards, *Quantitative Seismology*, University Science Books, Sausalito, CA, USA, 2nd edition, 2002.
- [4] J. C. Li, G. W. Ma, and J. Zhao, "An equivalent viscoelastic model for rock mass with parallel joints," *Journal of Geophysical Research:Solid Earth*, vol. 115, no. 3, 2010.
- [5] S. C. Bandis, A. C. Lumsden, and N. R. Barton, "Fundamentals of rock joint deformation," *International Journal of Rock Mechanics and Mining Sciences & Geomechanics Abstracts*, vol. 20, no. 6, pp. 249–268, 1983.
- [6] J. C. Li and G. W. Ma, "Experimental study of stress wave propagation across a filled rock joint," *International Journal of Rock Mechanics and Mining Sciences*, vol. 46, no. 3, pp. 471–478, 2009.
- [7] S. J. Reza, T. Zaniar, and D. T. Mihailo, "A note on the surface motion of a semi-cylindrical canyon for incident cylindrical SH waves radiated by a finite fault," *Earthquake Engineering and Engineering Vibration*, vol. 15, no. 3, pp. 445–455, 2016.
- [8] L. J. Pyrak-Nolte, L. R. Myer, and N. G. W. Cook, "Anisotropy in seismic velocities and amplitudes from multiple parallel fractures," *Journal of Geophysical Research*, vol. 95, no. 7, pp. 345–358, 1990.
- [9] Y. Jin, B. Song, Q. Qian et al., "Propagation of P-wave in dual nonlinear elastic medium for jointed rock mass," *Chinese Journal of Rock Mechanics and Engineering*, vol. 30, no. 12, pp. 2463–2473, 2011.
- [10] L. Tingting, L. I. Xinpin, L. I. Haibo et al., "Numerical study on stress wave propagation across filled joints," *Chinese Journal of Rock Mechanics and Engineering*, vol. 35, no. S2, pp. 3552–3560, 2016.
- [11] W. Yuan, W. Wang, X. Su et al., "Numerical study of the impact mechanism of decoupling charge on blasting-enhanced permeability in low-permeability sandstones," *International Journal of Rock Mechanics and Mining Sciences*, vol. 106, pp. 300–310, 2018.
- [12] L. F. Fan and H. Y. Sun, "Seismic wave propagation through an in-situ stressed rock mass," *Journal of Applied Geophysics*, vol. 121, no. 1, pp. 13–20, 2015.

- [13] X. Li, Z. Zhou, Z. Ye et al., "Study of rock mechanical characteristics under coupled static and dynamic loads," *Chinese Journal of Rock Mechanics and Engineering*, vol. 33, no. 10, pp. 2095–2100, 2014.
- [14] L. Wang, *Foundation of Stress Wave*, National Defense Industry Press, Beijing, China, 2005.
- [15] S. Chai, J. Li, and H. Li, "Propagation characteristics of cylindrical wave in joint rock masses," *Chinese Journal of Rock Mechanics and Engineering*, vol. 33, no. 3, pp. 523–530, 2014.
- [16] J. C. Li, "Wave propagation across non-linear rock joints based on time-domain recursive method," *Geophysical Journal International*, vol. 193, no. 2, pp. 970–985, 2013.
- [17] L. Zhang, *Test on the Performance of Blasting Equipment and Explosion Effect*, University of Science and Technology of China Press, Hefei, Anhui, China, 2006.
- [18] J. P. Zhao, *Experimental study on test and identification of blast wave in adjacent area to a borehole in concrete model and its action*, Ph.D thesis, Central South University of Technology, Changsha, Hunan, 2019.
- [19] F. H. Kulhawy, "Stress deformation properties of rock and rock discontinuities," *Engineering Geology*, vol. 9, no. 4, pp. 327–350, 1975.
- [20] G. Wang and C. Li, "Propagation law of stress wave in nonlinear structural surface medium," *Rock and Soil Mechanics*, vol. 30, no. 12, pp. 3747–3752, 2009.
- [21] W. Yuan, X. Su, W. Wang, L. Wen, and J. Chang, "Numerical study of the contributions of shock wave and detonation gas to crack generation in deep rock without free surfaces," *Journal of Petroleum Science and Engineering*, vol. 177, pp. 699–710, 2019.
- [22] Z. Zhu, S. Qian, L. Xianlun et al., "Study on crack initiation mechanism of three gorges granite," *Chinese Journal of Rock Mechanics and Engineering*, vol. 26, no. 12, pp. 2570–2575, 2007.



Hindawi

Submit your manuscripts at
www.hindawi.com

